Self-consistent description of multipole strength: Systematic calculations

J. Terasaki
School of Physics, Peking University, Beijing 100871, People's Republic of China

J. Engel
Department of Physics and Astronomy, University of North Carolina, Chapel Hill, North Carolina 27599-3255, USA
(Received 28 March 2006; published 3 October 2006)

We use the quasiparticle random-phase approximation with a few Skyrme density functionals to calculate strength functions in the $J^\pi = 0^+, 1^-$, and 2^+ channels for even Ca, Ni, and Sn isotopes from the proton drip line to the neutron drip line. We show where and how low-lying strength begins to appear as N increases. We also exhibit partial energy-weighted sums of the transition strength as functions of N for all nuclei calculated and transition densities for many of the interesting peaks. We find that low-energy strength increases with N in all multipoles, but with distinctive features in each. The low-lying 0^+ strength at large N barely involves protons at all, with the strength coming primarily from a single two-quasineutron configuration with very large spatial extent. The low-lying 1^- strength is different, with protons contributing to the transition density in the nuclear interior together with neutrons at large radii and with somewhat more collectivity in the heavier isotopes. The low-lying 2^+ transition strength goes largely to more localized and frequently more collective states. In all channels the correlation between strength and collectivity is much weaker than in stable nuclei. The three Skyrme interactions we test produce similar results, differing most significantly in their predictions for the location of the neutron drip line, the boundaries of deformed regions, energies of and transition strengths to the lowest 2^+ states between closed shells, and isovector energy-weighted sum rules.

DOI: 10.1103/PhysRevC.74.044301 PACS number(s): 21.10.Pc, 21.60.Jz

I. INTRODUCTION

Very unstable nuclei with unusual ratios of neutron number (N) to proton number (Z) are currently the subject of intense theoretical and experimental work. The effect of excess neutrons and the accompanying low-lying continuum on nuclear properties is particularly important. In ground states these conditions sometimes lead to halos, thick skins, and changes in magic numbers. Less is known about excited states, which we study here by calculating transition strengths and densities.

Most of the work on excited states is in light neutron-rich nuclei; a low-energy strength-function peak has been studied for years. Recent work has focused on enhanced 1^- strength in nuclei such as ^{11}Li or in neutron-rich oxygen isotopes [1–11]. But in heavier nuclei, calculations are more spotty. Several groups have calculated the isovector (IV) 1^- strength functions, or photoabsorption cross sections, in the Ca isotopes [5,10,12–15]. (For experiments in stable isotopes, see Ref. [16] and references therein.) The method we use here, the quasiparticle random-phase approximation (QRPA), has been applied mainly to selected 1^- excitations in particular isotopes of O, Ca, and Ni; one example is Ref. [10], which asserts that the low-energy excitations reflect strong particle-particle ("dineutron") correlations. References [17,18] present extensive and systematic QRPA calculations of photoabsorption cross sections but focus primarily on radiative neutron-capture cross sections. The relativistic QRPA [8,19–21] has been applied more with an eye to nuclear structure issues (for a recent review, see Ref. [22]), asserting, for example, that low-lying isoscalar (IS) 1^- states exhibit toroidal flow. References [23,24] go beyond RPA, altering details of predicted low-lying strength.

Other channels have been discussed less than the IV 1^-. The authors of Ref. [25] calculate 0^+ strength functions in Ca isotopes up to the neutron drip line, finding an enhancement at low energy in ^{60}Ca. Reference [26] examines transition strengths in the 0^+, 1^-, and 2^+ channels near the neutron drip line, finding, for example, a sharp 2^+ peak near $E = 0$ in ^{110}Ni.

The above represents a considerable amount of work on excitations in exotic nuclei, even if no comprehensive study exists. The conclusions so far can be summarized, roughly, as follows: (i) Low-energy strength grows as N increases; (ii) in very neutron-rich nuclei, the low-energy IV 1^- excitations often do not seem collective [27], i.e., they do not contain more than a few particle-hole or two-quasiparticle configurations; (iii) the corresponding transition densities have long neutron tails extending beyond the bulk nuclear radius; (iv) the neutron skin thickness is correlated with the amount of low-energy IV strength [28]; and (v) calculations reproduce measured amounts of low-energy strength [16,29] fairly well if they include many-particle many-hole correlations [15,23,24].

Most of this work focuses on nuclei right at the drip line and, as already noted, emphasizes the IV 1^- channel. It is still not known whether theory makes similar predictions for other neutron-rich nuclei or to what extent the properties of the low-energy peaks vary from one multipole to another. A typical open question: At what value of N does low-energy strength set in? References [5,14], which both predict a small IV 1^- peak at around $E = 9$ MeV in ^{60}Ca, differ on the question of whether there is any similar peak in ^{48}Ca. The purpose of this article is to provide a more comprehensive analysis, to calculate strength

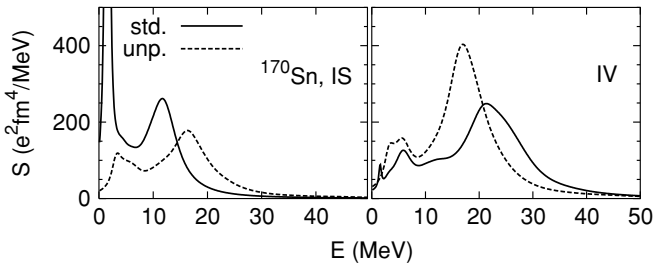

FIG. 1. QRPA (solid) and unperturbed (dashed) strength functions in the IS (left) and IV (right) 2^+ channels of the near-drip-line nucleus ^{170}Sn, with the interaction SkM*.

functions and transition densities in as many even-even nuclei as possible—Ca, Ni, and Sn isotopes from the proton drip line to the neutron drip line—in all natural-parity multipoles up to 2^+, so that we can seriously investigate how strength moves and changes its character as N and the multipolarity change. We display results in detail and examine the extent to which they depend on the effective interaction we use. Our tool is the QRPA with Skyrme density functionals (which we refer to as interactions) and density-independent delta pairing. The QRPA is currently the most sophisticated method that can be used for systematic calculations of this sort, at least without assuming that part of the nucleus is inert.

Section II describes our method. Section III shows strength functions in the three isotopic chains, looking for (N, Z)-dependent trends in their behavior and then transition densities to interesting states, in each of the three channels we examine. Section IV is a conclusion.

II. CALCULATION

Our approach to the QRPA is described in detail in Ref. [30], and we discuss it here only briefly. The starting point is a coordinate-space Hartree-Fock-Bogoliubov (HFB) calculation, with spherical symmetry assumed, carried out with the code used in Refs. [31,32]. The code outputs quasiparticle wave functions. We take the continuum into account by placing the nucleus in a spherical box with radius 20 fm, the largest value allowing QRPA calculations over a wide range of nuclei. We use as large a single-particle space as possible—an HFB quasiparticle-energy cutoff of 200 MeV—and solve the HFB equations accurately to ease the removal of spurious states from the QRPA and satisfy sum rules.

Next we diagonalize the HFB density matrix to obtain a set of canonical states—as many as there are quasiparticle states—pairs of which make up our two-quasiparticle QRPA basis. There is a limit to the number of QRPA states we can handle so we truncate the set of canonical states as follows: For $N < 82$ we limit the single-particle angular momentum to $j < 15/2$, and for $N \geqslant 84$ we take $j < 21/2$. If the ground state has a finite pairing gap in the HFB calculation we omit from the QRPA canonical states with very small occupation probability v_μ^2. In the $J^\pi = 0^+$ and 1^- channels we omit states with $v_\mu^2 < 10^{-12}$, and in the $J^\pi = 2^+$ channel we omit those with $v_\mu^2 < 10^{-8}$. If the mean field has no pairing we use the Hartree-Fock energy to truncate; in the $J^\pi = 0^+$ and 1^- channels we omit canonical states with energy $\varepsilon_\mu > 150$ MeV, and in the $J^\pi = 2^+$ channel we omit those with $\varepsilon_\mu > 100$ MeV.

With this basis, we construct the QRPA-Hamiltonian matrix, which contains off-diagonal elements from the one-quasiparticle Hamiltonian as well as the matrix elements of

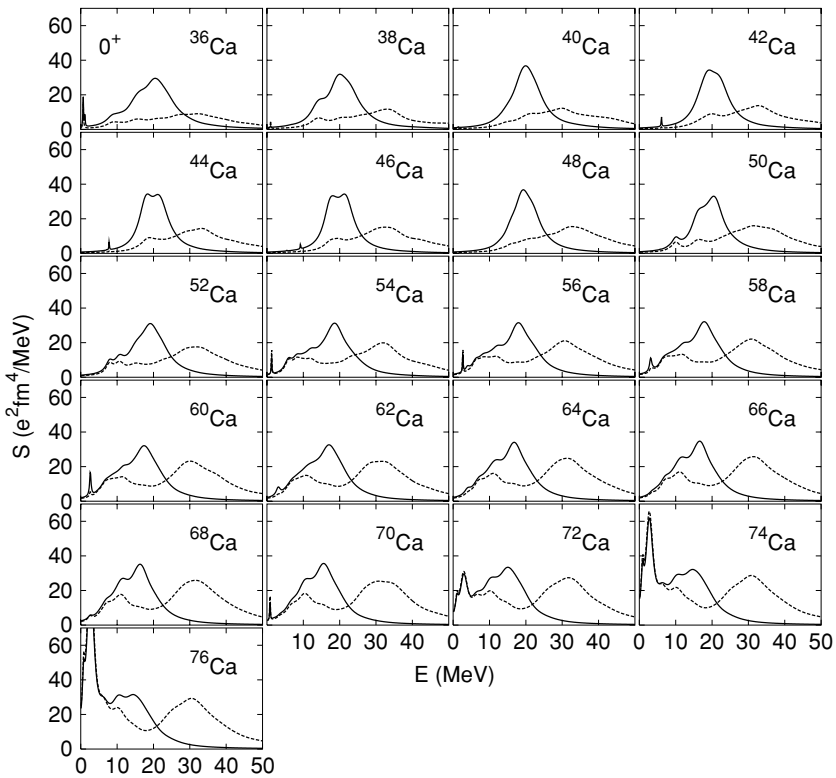

FIG. 2. IS (solid) and IV (dashed) 0^+ strength functions for even Ca isotopes (SkM*).

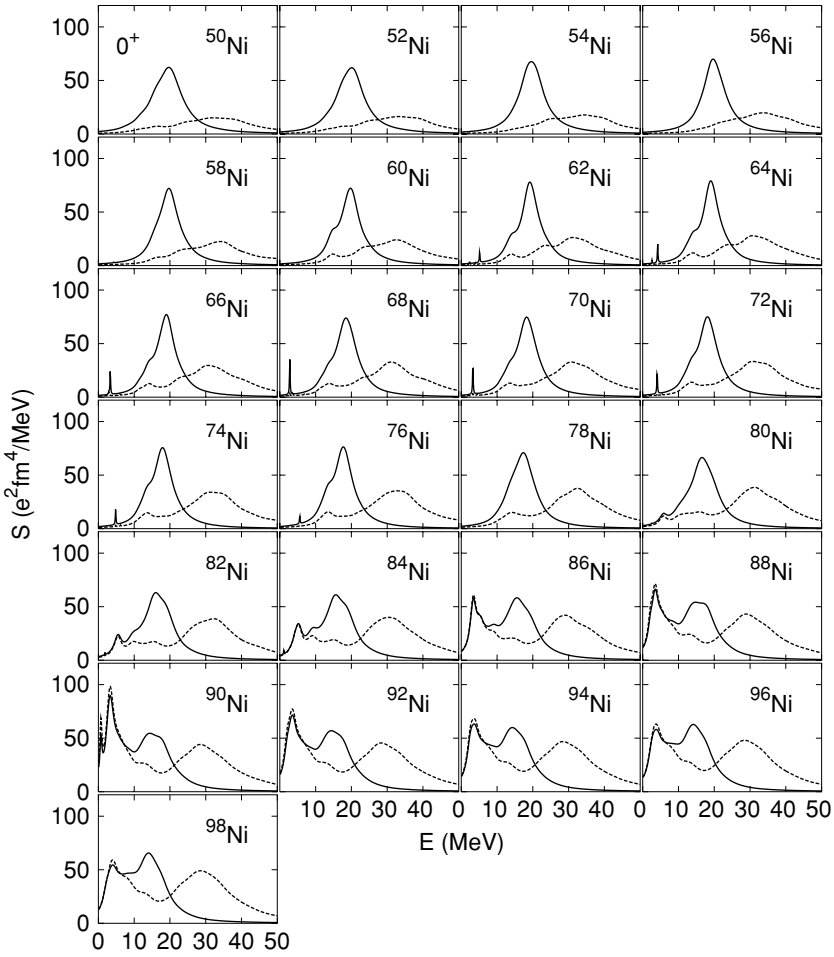

FIG. 3. The same as Fig. 2 but for Ni isotopes.

the residual two-body interaction. These matrix elements are functional derivatives of the energy with respect to the density and pairing tensor. After diagonalizing the QRPA Hamiltonian, we use the eigenvectors to obtain strength functions [33] and transition densities (see Appendix).

The largest matrix dimension that we encounter here (in the 1^- channel for Sn near the neutron drip line) is about 14,000, and the smallest is about 2,000 (in the 0^+ channel for Ca near the proton drip line).[1] The separation of spurious excitations from physical states is as complete as in Ref. [30] in most of cases, and all double-commutator sum rules are exhausted essentially completely at 100 MeV or less of excitation energy.

We use three Skyrme interactions: SkM*, SLy4, and SkP. Our pairing interaction has zero range with no density dependence (this is often called "volume pairing"). There is no stable HFB solution with SkP for Ca and Ni isotopes. The problem is analyzed in Ref. [34] and attributed to a large isovector gradient term. The other interactions do not have this problem, but they give solutions that are unstable against QRPA quadrupole vibrations in isotopes with $N = 72$ in Ni (SkM*), $N = 104$–112 in Sn (SkM*), and $N = 60$–$64, 96$–110 in Sn (SLy4), and so we do not discuss those cases.

III. STRENGTH FUNCTIONS AND TRANSITION DENSITIES

A. Definitions

Strength functions are important because they capture information about all excited states and can often be measured. We define the strength functions through the transition operators $J^\pi = 0^+$:

$$\hat{F}^{\rm IS}_{00} = \frac{eZ}{A}\sum_{i=1}^{A} r_i^2,$$
$$\hat{F}^{\rm IV}_{00} = \frac{eN}{A}\sum_{i=1}^{Z} r_i^2 - \frac{eZ}{A}\sum_{i=1}^{N} r_i^2, \quad (1)$$

$J^\pi = 1^-$:

$$\hat{F}^{\rm IS}_{1M} = \frac{eZ}{A}\sum_{i=1}^{A} r_i^3\, Y_{1M}(\Omega_i),$$
$$\hat{F}^{\rm IV}_{1M} = \frac{eN}{A}\sum_{i=1}^{Z} r_i\, Y_{1M}(\Omega_i) - \frac{eZ}{A}\sum_{i=1}^{N} r_i\, Y_{1M}(\Omega_i), \quad (2)$$

[1] In Ref. [30], we used cutoffs of $v_\mu^2 = 10^{-12}$ and $\varepsilon_\mu = 150$ MeV for the 2^+ channel, and then the maximum dimension of the Hamiltonian matrix was about 20,000.

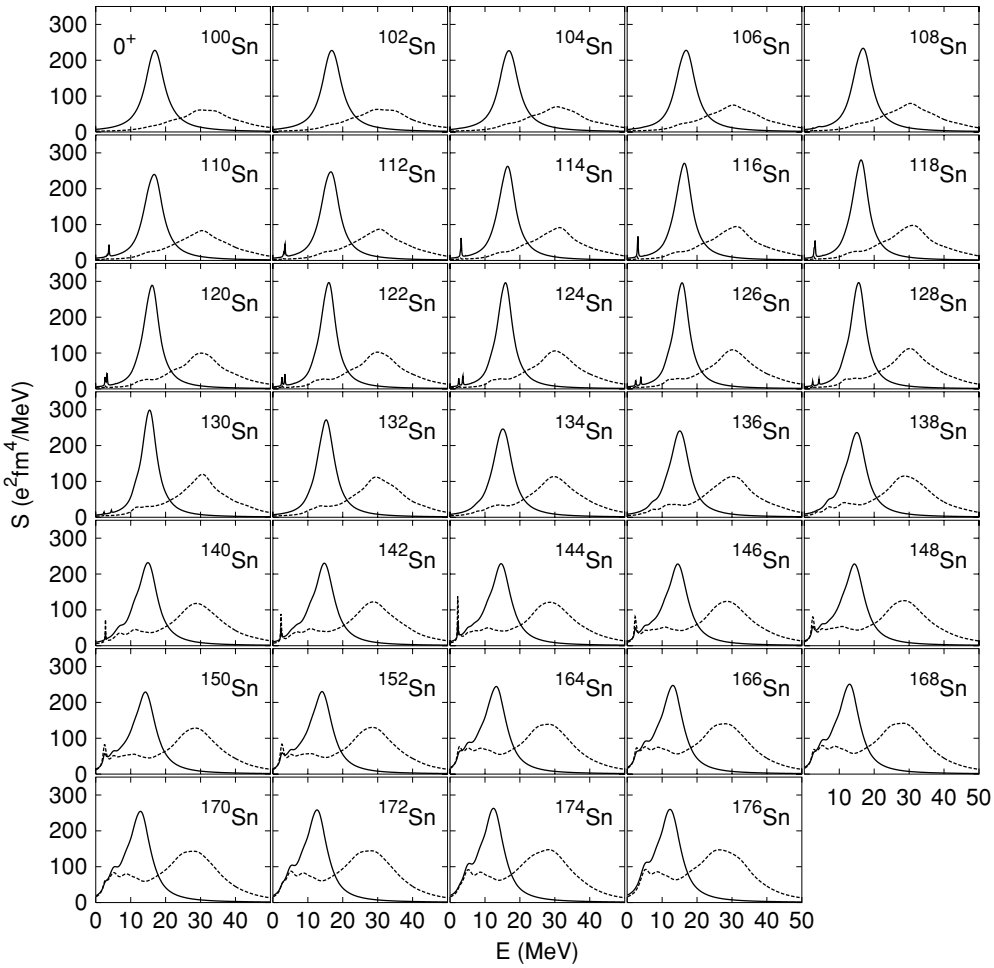

FIG. 4. The same as Fig. 2 but for Sn isotopes.

$J^\pi = 2^+$:

$$\hat{F}^{\rm IS}_{2M} = \frac{eZ}{A}\sum_{i=1}^{A} r_i^2\, Y_{2M}(\Omega_i),$$
$$\hat{F}^{\rm IV}_{2M} = \frac{eN}{A}\sum_{i=1}^{Z} r_i^2\, Y_{2M}(\Omega_i) - \frac{eZ}{A}\sum_{i=1}^{N} r_i^2\, Y_{2M}(\Omega_i), \quad (3)$$

where A is total-nucleon number and i is a single-particle index. The upper limit $Z(N)$ on a summation sign means that the sum is over protons (neutrons). The normalization of these operators is convenient for locating excitations that are due predominantly to neutrons. If that is the case, the IS and IV strengths are equal, except in the 1^- channel, where the operators depend on position differently.

To give an idea of the the size of QRPA corrections to unperturbed strength functions, we display in Fig. 1 the IS and IV 2^+ strengths in the near-drip-line nucleus ^{170}Sn, with and without the residual SkM* and the pairing interactions. The effects in the two channels are different: the IS interaction is attractive, and the IV interaction is repulsive.

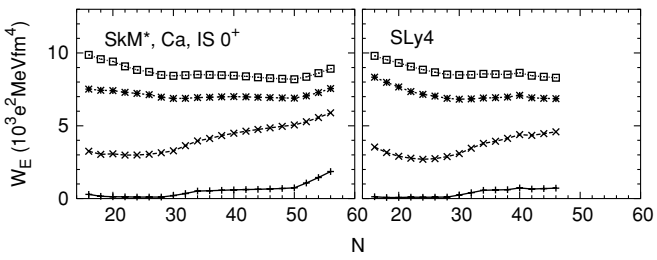

FIG. 5. N dependence of the partial energy-weighted sums in the IS 0^+ channel of Ca. The upper limits of the sums are 10 MeV (+), 20 MeV (x), 30 MeV (∗), and 100 MeV (□).

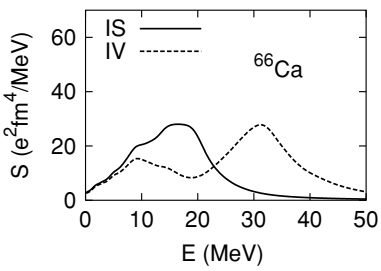

FIG. 6. 0^+ strength functions of ^{66}Ca (SLy4).

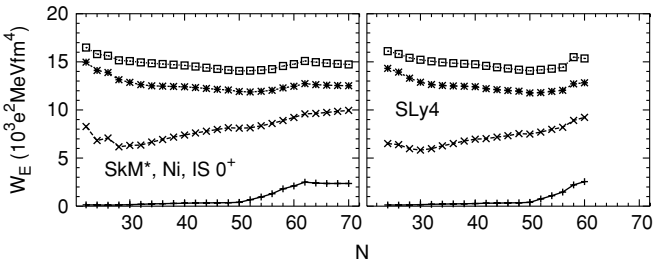

FIG. 7. The same as Fig. 5 but for Ni.

The transition density $\rho^q_{\rm tr}(\boldsymbol{r};k)$ to an excited state k is defined in the Appendix. Here we focus on the radial transition density

$$\rho^q_{\rm tr}(r;k) = r^2 \int d\Omega\, Y_{J_k M_k}(\Omega)\rho^q_{\rm tr}(\boldsymbol{r};k). \tag{4}$$

The transition amplitude depends on this quantity through the relation

$$\langle k|\hat{F}_{JM}|0\rangle = \int dr \sum_{q=p,n} f^q(r)\rho^q_{\rm tr}(r;k), \tag{5}$$

where $|0\rangle$ is the ground state and $f^q(r)$ is the radial part of the q component of the multipole operator $\hat{F}_{JM}$. The radial transition density therefore specifies the radius at which the strength is large or small. The transition density, as Eq. (A2) shows, is proportional to the product of particle and hole wave functions and so is localized as long as all hole states are localized, i.e., as long as the ground state is bound. We treat each multipole in turn in what follows. For each, we first show the strength functions, with spurious states removed, produced by SkM* and discuss those produced by the other Skyrme interactions when appropriate. We then display energy-weighted sums (up to several different energies) produced by all our interactions and finally examine transition densities to interesting states, focusing on low-lying peaks.

B. 0^+ channels

1. 0^+ *strength functions*

Figures 2–4 show the IS and IV strength functions in the $J^\pi = 0^+$ channels. In Ca (Fig. 2), most of the functions are smooth except for small low-energy spikes in several nuclei and the large low-energy peaks in ^{74,76}Ca. The IS giant resonances peak at $E = 20$ MeV for $^{36-52}$Ca and gradually move to 15 MeV by ^{76}Ca. As N increases a peak near $E = 0$ grows, becoming quite large at the drip line. The IV giant resonance is broad in the light isotopes and develops a low-energy component as N gets larger, apparently increasing the summed strength. The higher-energy peak moves only slightly over the same range of N. Near the drip line the low-energy IV strength develops a peak that exactly mirrors the IS peak, indicating that the strength in both channels is produced solely by neutrons. This distinct low-energy bump seems to appear first at 10 MeV in ^{50}Ca. This nucleus is not as short-lived as the isotopes near the drip line; perhaps the appearance of the low-energy mode is experimentally testable. The same nucleus marks the beginning of the low energy peak when we use SLy4.

The N dependence of the strength function of Ni (Fig. 3) is similar in many ways to that of Ca; the energy of the IS giant resonance, for example, falls in a similar way past $N = 40$. A large low-energy peak again develops near the neutron drip line, though not as dramatically as in Ca, and with the complication that the strength shrinks after ^{90}Ni. This peak first is noticeable in both the IS and IV channel at 6 MeV in ^{80}Ni, here and in calculations with SLy4. This example and that in Ca suggest more generally that the nucleus with two neutrons outside a closed shell will mark the appearance of the low-energy peak.

In Sn (Fig. 4), the peak near zero energy around the drip line is much smaller than those in Ca and Ni. The bump first appears in ^{136}Sn at $E = 8$ MeV (violating by two nucleons the conjecture made a few lines up) in both the IS and IV channels. This threshold nucleus is the same with other Skyrme interactions.

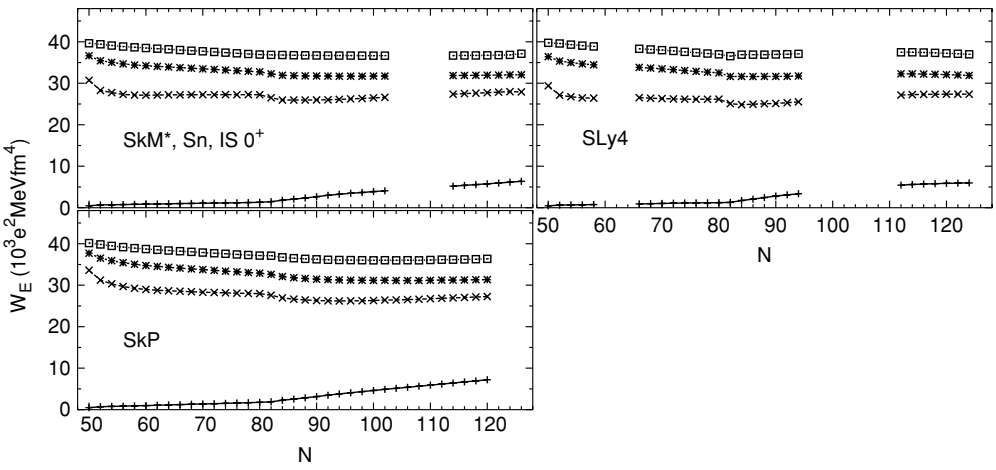

FIG. 8. The same as Fig. 5 but for Sn.

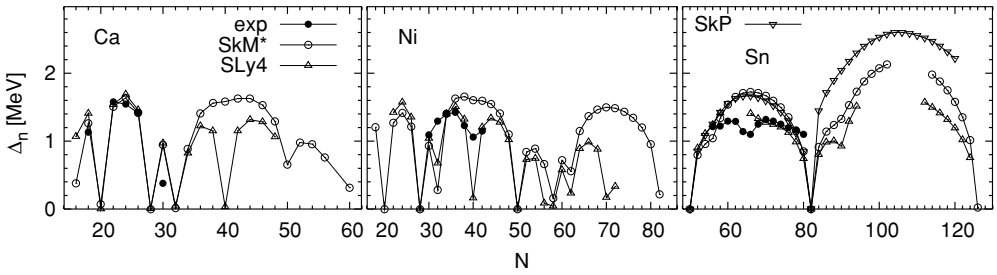

FIG. 9. Predictions of the Skyrme interactions for neutron pairing gaps in the Ca, Ni, and Sn isotope chains, along with data from measured odd-even mass differences [41].

Although we can make these kinds of comparisons in words, we display the results of both (or all three where possible) Skyrme interactions in a more quantitative and graphic way. To limit the number of our figures, we do so by showing predictions for the sum of energy-weighted strength up to four successively higher energies. We define the "partial" sum to energy E as

$$W_E = \int_0^E dE'\, E' S(E'), \tag{6}$$

where $S(E')$ is a strength function[2] (see Eq. (1) of Ref. [30]). Figure 5 shows W_E with $E = 10$, 20, 30, and 100 MeV for the IS 0^+ channel in Ca. All Skyrme interactions show similar N dependence and E dependence; the difference between the $E = 30$ and 100 MeV curves is comparable with or smaller than the differences among the other curves (separated by 10 MeV), reflecting the eventual vanishing of the strength as E increases. The $E = 20$ MeV curve increases more rapidly with N than the others for $N > 30$, indicating that the strength around $E = 20$ MeV is shifted down at large N.

The differences among the interactions are most apparent in the location of the neutron drip line, a static property; SLy4 predicts a very different drip line, at ^{66}Ca. Figure 6 displays both the IS and IV SLy4 strength functions in that nucleus. Apparently they are similar not to those of the SkM* drip-line nucleus ^{76}Ca but rather to those of the SkM* ^{66}Ca (see Fig. 2). Clearly the quantum numbers of the quasiparticle orbits involved in the transition affect the strength much more than the neutron separation energy. Analysis of the transition densities, which we discuss next (though not for this particular example), bear this conclusion out. Overall differences in strength functions produced by the two interactions in the same nucleus, when both are predicted particle-stable, are minor.

In the IV channel, the trends in partial sums are simpler (uniform increase with N for all interactions) but SkM* produces 10%–15% more integrated strength than SLy4.[3] To see how the total energy-weighted strength can differ from one interaction to another, we examine the IV energy-weighted sum rule (EWSR)

$$\sum_k \sum_M E_k \left| \langle k | \hat{F}^{\mathrm{IV}}_{JM} | 0 \rangle \right|^2 = S_{\mathrm{EW}}(J) + C_c I_c(J), \tag{7}$$

$$S_{\mathrm{EW}}(0) = \frac{2e^2\hbar^2}{m} \left\{ \frac{N^2 Z}{A^2} \langle r^2 \rangle_p + \frac{Z^2 N}{A^2} \langle r^2 \rangle_n \right\}, \tag{8}$$

[2]Equation (6) overestimates the energy-weighted sum slightly if the strength function has a large peak at low energy. The reason is that an unavoidable tail at negative energies (due to the folding of discrete peaks) is not included. The problem is most severe near the drip line, resulting in errors of at most 10%. We have used the EWSR values for W_E at the largest E in the figures, so that no strength at all is neglected there.

[3]Figures of W_E in the IV channels, omitted here to save space, are shown in Ref. [35].

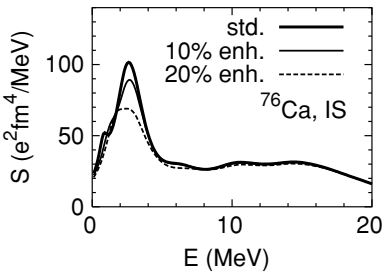

FIG. 10. Effect of 10% (thin line) and 20% (dashed line) increase of the pairing-interaction strength on the IS 0^+ strength function of ^{76}Ca, with SkM*. The thick line represents no increase.

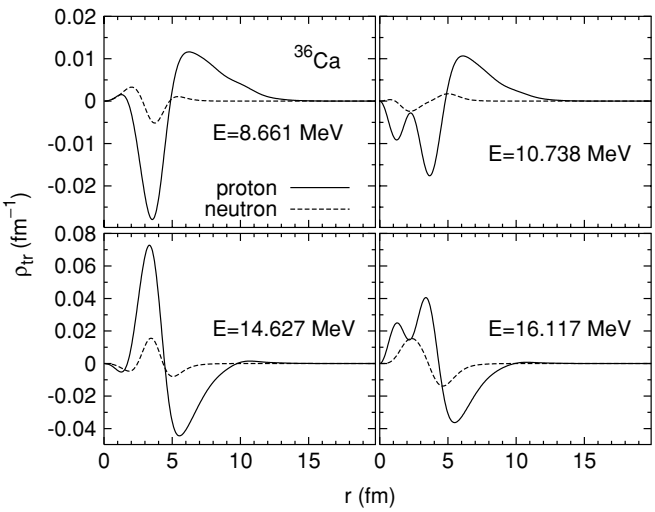

FIG. 11. Proton and neutron transition densities to the four states in ^{36}Ca in the peaks of the strength function ($E < 17$ MeV) in Fig. 2.

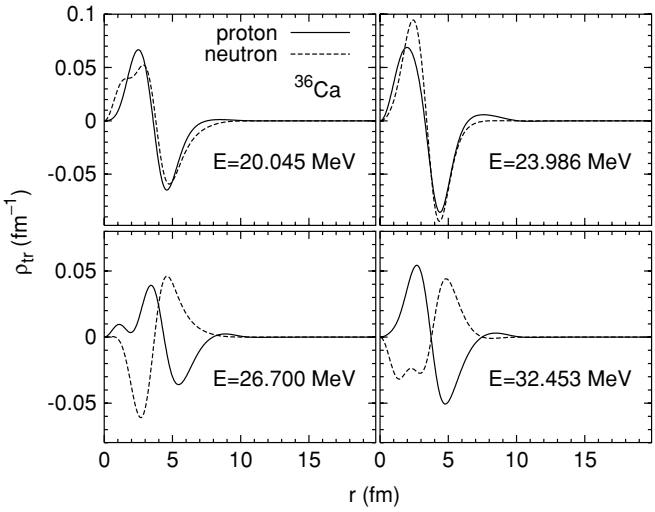

FIG. 12. The same as Fig. 11 but for the giant resonances. The states in the upper panels correspond to the peaks of the IS giant resonance and in the lower to the IV giant resonance.

$$S_{\rm EW}(J \geqslant 1) = \frac{e^2\hbar^2}{8\pi m} J(2J+1)^2 \times \left\{ \frac{N^2 Z}{A^2} \langle r^{2J-2} \rangle_p + \frac{Z^2 N}{A^2} \langle r^{2J-2} \rangle_n \right\}, \quad (9)$$

$$C_c = \tfrac{1}{4}(t_1 + t_2) + \tfrac{1}{8}(t_1 x_1 + t_2 x_2), \quad (10)$$

$$I_c(J) = e^2 \sum_M \int d^3\boldsymbol{r}\, |\nabla f_{JM}(\boldsymbol{r})|^2 \rho_0^n(\boldsymbol{r}) \rho_0^p(\boldsymbol{r}), \quad (11)$$

$$f_{00}(\boldsymbol{r}) = r^2, \quad (12)$$

$$f_{JM}(\boldsymbol{r}) = r^J Y_{JM}(\Omega), \quad J \geqslant 1. \quad (13)$$

Here E_k is the energy of $|k\rangle$, m is the nucleon mass, and $\langle r^2 \rangle_p (\langle r^2 \rangle_n)$ is the mean square proton (neutron) ground-state radius. The sum over states k does not include spurious states. The second term $C_c I_c(J)$ in Eq. (7), with $\rho_0^p(\boldsymbol{r})$ and $\rho_0^n(\boldsymbol{r})$ of Eq. (11) the proton and neutron ground-state densities, is a correction arising from the momentum-dependent terms of the Skyrme interaction. The Skyrme parameters t_0, t_1, etc., are defined in Refs. [36] (SkM*), [37] (SLy4), and [31] (SkP). Another term in the sum rule, depending on the proton-neutron mixed density, is always zero in our work.

In Table I we show $S_{\rm EW}(0)$, C_c, $I_c(0)$, and EWSR (the full energy-weighted sum) for ^{60}Ca. The interactions reproduce ground-state observables about equally well, so the difference in the EWSR, as the table shows, comes from the term involving C_c. The degree by which the EWSR exceeds $S_{\rm EW}(J)$ is similar to that found in other calculations (see, e.g., Chapter 10 of Ref. [38] and Refs. [37,39]).

TABLE I. Contributions to the summed energy-weighted strength in the IV 0^+ channel of ^{60}Ca.

Interaction	$S_{\rm EW}(0)$ (e^2 MeV fm^4)	C_c (MeV fm^5)	$I_c(0)$ (e^2/fm)	Energy-weighted sum (e^2 MeV fm^4)
SkM*	15587	68.74	58.01	19575
SLy4	15722	32.47	57.90	17602
SkP		44.64		

The properties of Ni are similar to those of Ca. $W_{E=20\,\rm MeV}$ in the IS channel of Ni increases more rapidly than the other curves (Fig. 7). The N dependence is again monotonic in the IV channel, and SkM* again has the larger IV sum-rule value. $W_{E=20\,\rm MeV}$ in the IS channel of Sn is much higher than $W_{E=10\,\rm MeV}$ (Fig. 8), reflecting the lower energy of the giant resonance. The IV sum rules follow the same order as in the other isotopes, with SkP slightly larger than SLy4.

Before proceeding to transition densities, we should comment on the effects of pairing. Though a comprehensive investigation is beyond the scope of this article, we do show the predictions of the various Skyrme interactions for neutron pairing gaps, along with empirical values from odd-even mass differences, in Fig. 9. Though the pairing strength is fit to odd-even mass differences (extracted in the same way as in Ref. [40]) in all these isotopes, separately for each interaction, it appears to work best in Ni and Sn in combination with SLy4.

To get an idea of what variations in pairing do, we show in Fig. 10 the effects of increasing the pairing strength by 10% and 20% on the IS 0^+ strength below 20 MeV in the drip-line nucleus ^{76}Ca. Even a 10% change, however, is larger than the data allow; it nearly doubles the pairing gap.

2. 0^+ transition densities

Figure 11 shows the transition densities to four states with large strengths below the giant resonances in ^{36}Ca (the energies label the results of the QRPA calculation before smoothing). Proton excitations are important, particularly because of the factor r^2 in the 0^+ transition operator. The root-mean-square (rms) radii of the protons and neutrons in the ground state are 3.40 and 3.19 fm. The important part for the strength comes from outside the rms radius.

This is not true of the giant resonances. Figure 12 shows transition densities in the peaks of the giant resonances of ^{36}Ca. The upper two panels represent the IS giant resonance, and as expected the protons and neutrons have similar transition densities. In the lower panels, corresponding to the IV giant resonance, the two densities are out of phase. The peaks of the proton transition densities are closer to the center of the nucleus than those of the lower-energy states, particularly in the IS channel.

We saw that a low-energy bump appeared after magic numbers in neutron-rich nuclei. In Ca, the relevant isotope is ^{50}Ca. Figure 13 shows that the excitation is created entirely by neutrons. But the state is not at all collective. The largest two-quasiparticle component in the QRPA wave function is $\nu 3p_{3/2}(\mathcal{E}_\mu = 9.175\,\text{MeV}, \bar{v}_\mu^2 = 6.0 \times 10^{-4}) \otimes \nu 2p_{3/2}(\mathcal{E}_\mu = 0.880\,\text{MeV}, \bar{v}_\mu^2 = 0.488)$, where $\mathcal{E}_\mu$ is the quasiparticle energy in the HFB quasiparticle basis, $\bar{v}_\mu^2$ is the diagonal ground-state occupation probability (norm of the lower component of the quasiparticle wave function), and the radial quantum numbers are assigned in order of $\mathcal{E}_\mu (-\mathcal{E}_\mu$ for those having $\bar{v}_\mu^2 > 0.5)$.

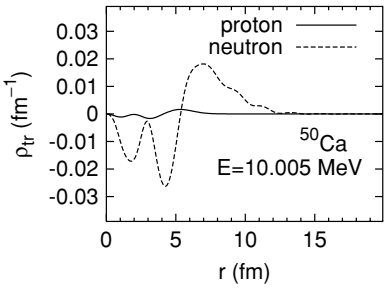

FIG. 13. Transition densities to the excited state in the small low-energy bump of the 0^+ strength function in ^{50}Ca.

This component is nearly the entire wave function; its squared amplitude $\bar{X}^2_{\mu\nu} - \bar{Y}^2_{\mu\nu}$ (where $\bar{X}_{\mu\nu}$ and $\bar{Y}_{\mu\nu}$ are the forward and backward amplitudes of the QRPA solution) is 0.98. The component corresponds to the excitation of a neutron from a $p_{3/2}$ orbit near the Fermi surface, and strongly affected by pairing correlations, to another $p_{3/2}$ orbit about 9 MeV above. The two-quasiparticle energy is 10.055 MeV and the energy of the excited state itself 10.005 MeV, so the excitation is almost unaffected by the residual interaction. Yet this nearly pure two-quasiparticle state, because the neutron transition density has such a long tail, carries 5% of the total IS transition strength. Furthermore, protons contribute essentially nothing to the transition; the maximum of the $\bar{X}^2_{\mu\nu} - \bar{Y}^2_{\mu\nu}$ for protons is 0.3×10^{-4}. This remarkable situation—dominance by a single two-neutron-quasiparticle configuration with very large strength—occurs in the 0^+ channel repeatedly.

Take, for example, the drip-line nucleus ^{76}Ca. Two low-lying states, at $E = 2.391$ and 2.995 MeV, together account for 26% of the total IS strength and 10% of the EWSR. Transition densities, shown in Fig. 14, are again dominated by neutrons, with outer peaks at 9–11 fm. The rms ground-state radii are 3.74 fm for protons and 4.62 fm for neutrons, so the highest (inner) peaks of $\rho_{\rm tr}(r;k)$ are close to the neutron rms radius. The main two-quasiparticle component of the excited state with $E = 2.391$ MeV has a squared amplitude of 0.82 and the main component of the state at $E = 2.995$ MeV has a squared amplitude of 0.93. As previously, these are nearly pure two-quasineutron excitations with long tails in their product.

Turning now to Ni near the closed $N = 50$ shell, we see that ^{80}Ni has a small bump around 5 MeV, whereas ^{78}Ni does not (Fig. 3). The situation in the first nucleus is similar to that of the neutron-rich Ca isotopes; the main component

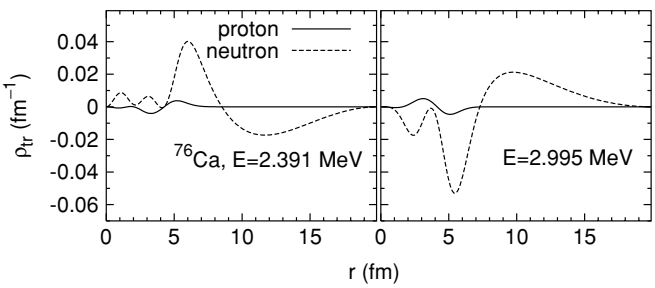

FIG. 14. Transition densities to the two excited states in the low-energy peak of the 0^+ strength functions in ^{76}Ca.

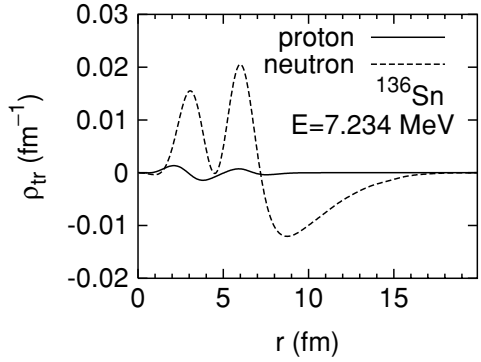

FIG. 15. Transition densities to the excited state in a small bump in the 0^+ strength function of ^{136}Sn.

in the bump has $\bar{X}^2_{\mu\nu} - \bar{Y}^2_{\mu\nu} = 0.76$ and transition densities are almost identical in shape (though not quite as extended) as those in the right-hand side of Fig. 14. At the drip-line nucleus ^{98}Ni, the main component of the excited state at $E = 3.452$ MeV has $\bar{X}^2_{\mu\nu} - \bar{Y}^2_{\mu\nu} = 0.82$, again very large.

In Sn the nucleus just past the closed neutron shell is ^{134}Sn. Here, as we noted earlier, a new bump is not visible (Fig. 4), until ^{136}Sn. We show the transition density to the corresponding state in Fig. 15. The excitation's main component is $\nu 2f_{7/2}(\mathcal{E}_\mu = 0.950$ MeV, $\bar{v}^2_\mu = 0.44) \otimes \nu 3f_{7/2}(\mathcal{E}_\mu = 6.302$ MeV, $\bar{v}^2_\mu = 6.2 \times 10^{-4})$, with $\bar{X}^2_{\mu\nu} - \bar{Y}^2_{\mu\nu} = 0.90$. The transition densities to low-energy states in the drip line nucleus ^{176}Sn are similar to those in their Ca and Ni counterparts.

We have not tried altering the density dependence of the pairing at all. A more thorough investigation of pairing effects is clearly in order.

We turn finally and very briefly to the dependence of the transition densities on the Skyrme interaction. SkM* and SLy4, unsurprisingly by now, give similar transition densities to states below the giant resonances in ^{36}Ca and to giant resonances everywhere. To compare the low-energy densities in neutron-rich isotopes, we include just Fig. 16, which shows the SLy4 transition densities to the states in the small low-energy bump in ^{50}Ca. The figure is not very different from that produced by SkM*, Fig. 13. In general, differences in low-lying transition densities produced by different interactions can be seen but are minor.

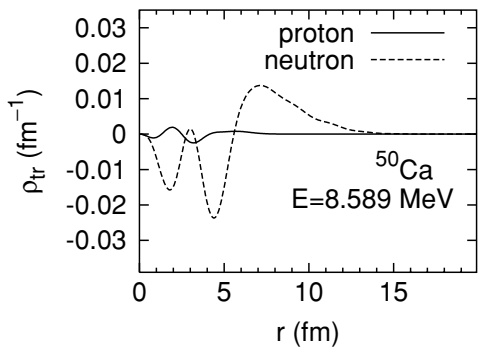

FIG. 16. Same as Fig. 13 but with SLy4.

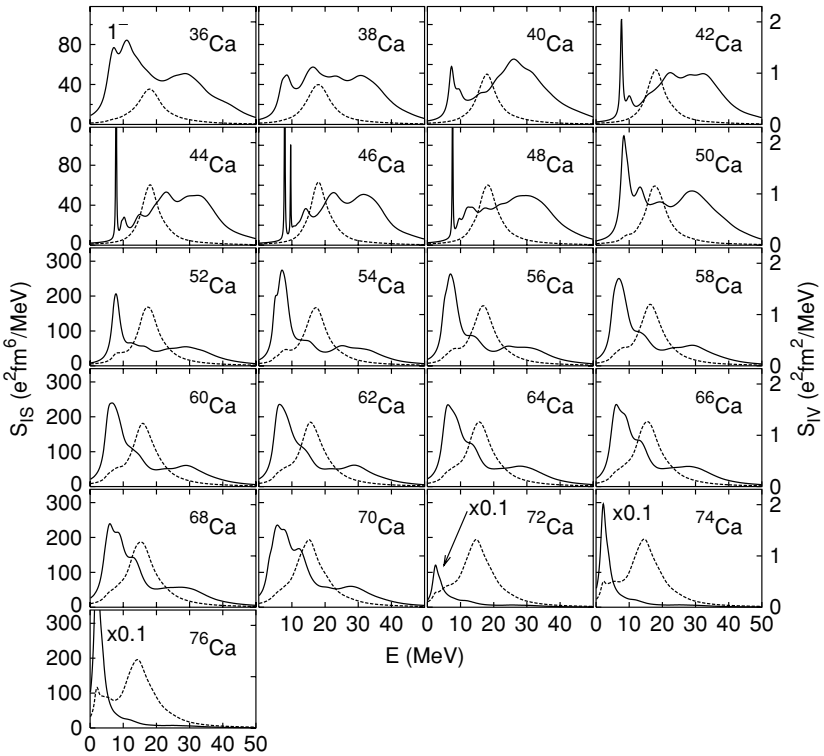

FIG. 17. IS (solid, scale on left) and IV (dashed, scale on right) 1^- strength functions for even Ca isotopes (SkM*). The IS strength functions in ^{72,74,76}Ca are reduced by a factor of 10.

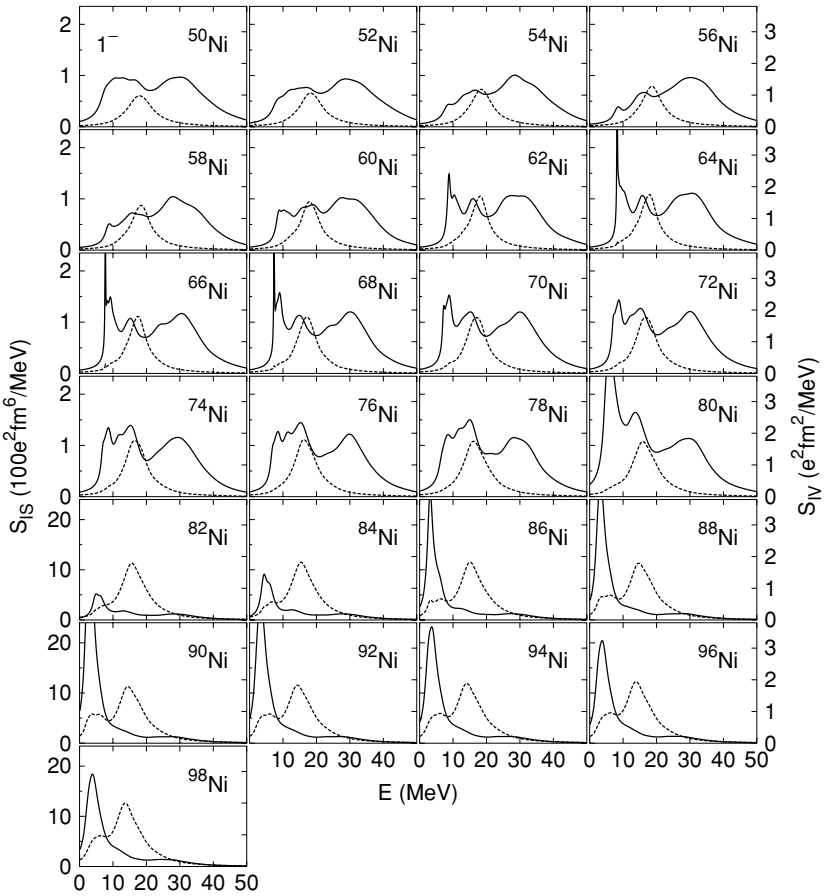

FIG. 18. IS (solid, scale on left) and IV (dashed, scale on right) 1^- strength functions for even Ni isotopes (SkM*).

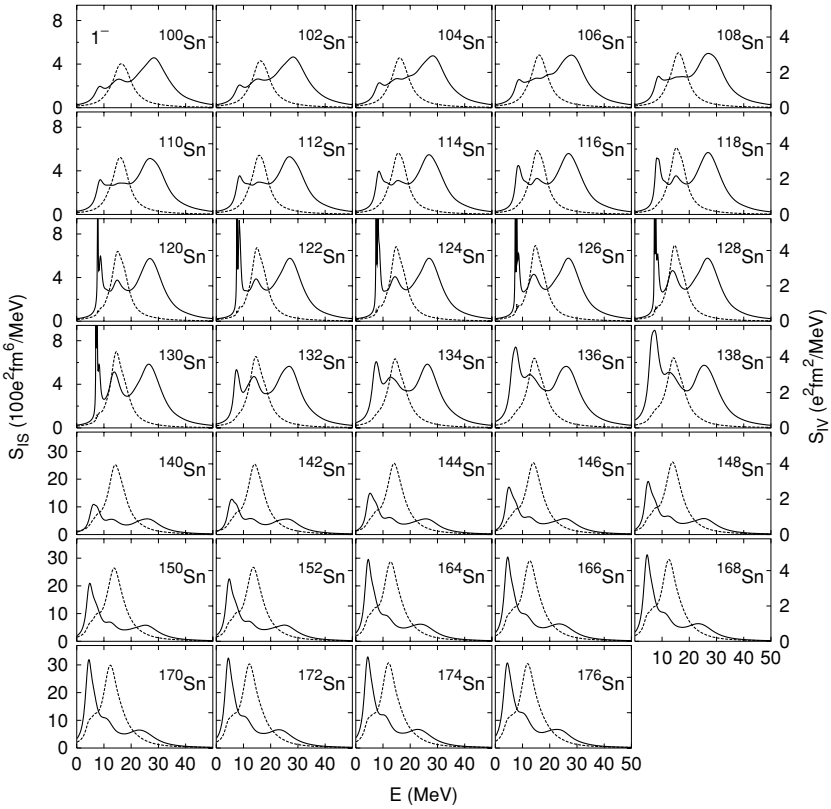

FIG. 19. The same as Fig. 18 but for Sn isotopes.

C. 1^- channels

1. 1^- *strength functions*

Having analyzed the 0^+ multipole in detail, we will, for the most part, let the higher-multipole strength-function figures speak for themselves (though we have more to say about transition densities). Just a few remarks about the 1^- channel: The IS strength functions in Ca appear in Fig. 17. Here, unlike in the 0^+ channel, there is a clear low-energy peak in all nuclei, increasing in size[4] after ^{48}Ca. (The IS strength functions of ^{72,74,76}Ca are multiplied by 0.1 in the figure.) In ^{76}Ca, 45% of the energy-weighted strength is below 10 MeV. The IV strength functions also increase with N at low energy. The small low-energy bump in ^{50}Ca is produced by SLy4 as well as SkM*.

We see similar N dependence in Ni (Fig. 18), though after ^{90}Ni the low-energy IS peak shrinks. The threshold for rapid growth with both Skyrme interactions is the closed-shell nucleus ^{78}Ni. In Sn, once again, the low-energy IS peak grows with N, though more smoothly than in the other isotopes (Fig. 19). In particular, there is apparently no sudden increase at the closed-shell-plus-two nucleus ^{134}Sn. Recently, Ref. [29] reported a clear IV bump around 10 MeV in ^{130,132}Sn. The bumps in our calculated spectra do not seem to really set in until higher N.

The 1^- W_E tell a slightly different story (Figs. 20–22), showing clear kinks. The partial sums in the IS channel of Sn (Fig. 22) bend noticeably at $N = 82$, clearly because of an increase in low-energy strength. As remarked above, the increase is not obvious in the strength-function figures. The choice of interaction makes very little difference in the W_E except in the blank regions (indicating quadrupole deformation) and near the neutron drip line.

[4]The low-energy peaks of $^{42-48}$Ca are so sharp because they are bound states.

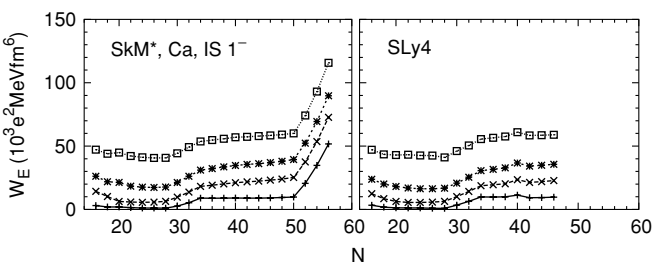

FIG. 20. The same as Fig. 5 but for the 1^- channel.

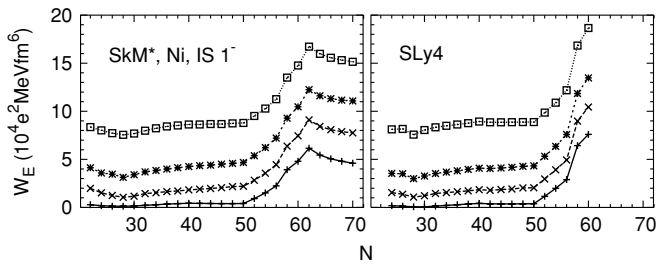

FIG. 21. The same as Fig. 7 but for the 1^- channel.

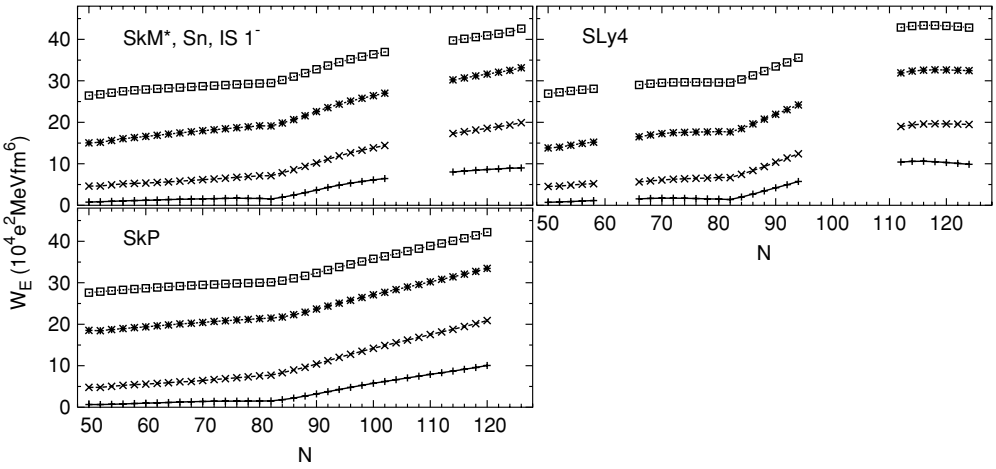

FIG. 22. The same as Fig. 8 but for the 1^- channel.

There are some experimental data [16] on ratios of partial energy-weighted IV sums up to $E = 10$ MeV to the EWSR values. These ratios, in ^{40,44,48}Ca, are $2.0(3) \times 10^{-4}$, $3.9(7) \times 10^{-3}$, and $3.3(4) \times 10^{-3}$. Our corresponding values wth SkM* are 9×10^{-4}, 2×10^{-6}, and 5×10^{-5}. The most obvious feature of both the experimental and calculated numbers is that they are small.

According to the analytical argument in Sec. III B1, if the IV EWSR depends on the interaction in one multipole, then it should in all multipoles. Though we do not display the sums, that is indeed the case.

2. 1^- *transition densities*

As we have just seen, the large neutron tails in the transition density are responsible for enhanced low-lying strength near the drip line. The robust enhancement of low-lying IS 1^- strength is due in large part to the factor r^3, which emphasizes large radii, in the transition operator. One stark difference between these transition densities and those of the 0^+ channel is the role played by protons, which is nonnegligible here. Another is the sometimes increased collectivity[5] of the neutrons. Figure 23 shows the transition densities of 2 states in the low-lying IS peak in ^{50}Ca. Protons and neutrons contribute coherently. The component of the state at $E = 8.228$ MeV with the largest amplitude is $\nu 2p_{3/2}(\mathcal{E}_\mu = 0.880$ MeV, $\bar{v}_\mu^2 = 0.49) \otimes \nu 1d_{3/2}(\mathcal{E}_\mu = 8.219$ MeV, $\bar{v}_\mu^2 = 0.98)$. The squared amplitude $\bar{X}^2_{\mu\nu} - \bar{Y}^2_{\mu\nu}$ is only 0.36. Two other configurations, $\nu 3s_{1/2} \otimes \nu 2p_{3/2}$ and $\pi 2p_{3/2} \otimes \pi 1d_{3/2}$, have $\bar{X}^2_{\mu\nu} - \bar{Y}^2_{\mu\nu} = 0.20$ and 0.12, not much smaller. And because the two-quasiparticle energy of the largest component is 9.099 MeV, the excited state gains more correlation energy than those in the 0^+ channel.

The proton contributions remain even at the neutron drip line. Figure 24 shows the transition densities to three excited states in the large low-energy IS peak in ^{76}Ca (Fig. 17). These states have IS strengths 9227 e^2 fm^6($E = 1.931$ MeV), 3219 e^2 fm^6($E = 2.199$ MeV), and 4856 e^2 fm^6($E = 3.501$ MeV), representing 42, 15, and 22% of the total strength. Although protons play no role for $r > 6$ fm, they are active around $r = 5$ fm. The main difference between these states and those of ^{50}Ca is that here the neutrons both extend much further out and contribute more than protons inside the nucleus. It is the tail that is mainly responsible for the increased strength.

Interestingly, the states in ^{76}Ca are mainly of two-quasiparticle character even though there is a coherent proton contribution. The component in the state at $E = 1.931$ MeV with the largest amplitude ($\bar{X}^2_{\mu\nu} - \bar{Y}^2_{\mu\nu} = 0.914$) is $\nu 3s_{1/2}(\mathcal{E}_\mu = 0.355$ MeV, $\bar{v}_\mu^2 = 0.64) \otimes \nu 3p_{3/2}(\mathcal{E}_\mu = 1.582$ MeV, $\bar{v}_\mu^2 = 0.59 \times 10^{-3})$. In the state at $E = 2.199$ MeV the component with the largest amplitude

[5]By collectivity, we mean the coherent contribution of two-quasiparticle configurations to the transition strength.

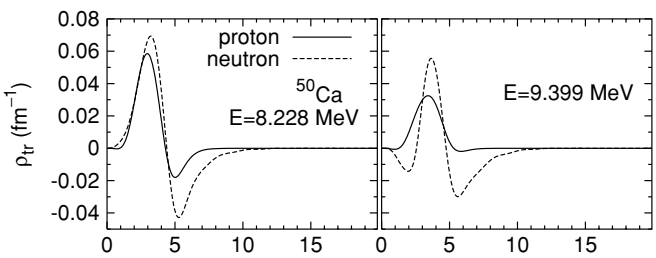

FIG. 23. Transition densities to the excited states in the low-energy peak of the IS 1^- strength function of ^{50}Ca.

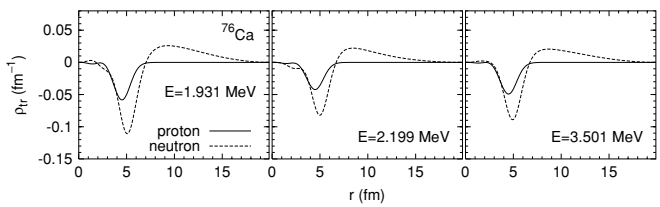

FIG. 24. Transition densities to the excited states in the low-energy peak of the IS 1^- strength function of ^{76}Ca.

TABLE II. Two quasineutron components of strong low-energy IV 1^- excited states in ^{132}Sn. The relativistic RPA results are from Ref. [8]. The percentages are the differences between the squared RPA forward amplitudes and backward amplitudes; only those larger than 1% are shown.

This work		Ref. [8]
8.0 MeV	8.6 MeV	8.6 MeV
$3s_{1/2} \to 3p_{1/2}(28.1\%)$	$2d_{3/2} \to 2f_{5/2}(63.0\%)$	$2d_{3/2} \to 2f_{5/2}(28.2\%)$
$2d_{3/2} \to 3p_{1/2}(26.6\%)$	$3s_{1/2} \to 3p_{1/2}(14.6\%)$	$2d_{5/2} \to 2f_{7/2}(21.9\%)$
$3s_{1/2} \to 3p_{3/2}(11.1\%)$	$1g_{7/2} \to 1h_{9/2}(5.6\%)$	$2d_{3/2} \to 3p_{1/2}(19.7\%)$
$1h_{11/2} \to 1i_{13/2}(6.9\%)$	$2d_{5/2} \to 2f_{7/2}(4.5\%)$	$1h_{11/2} \to 1i_{13/2}(10.5\%)$
$1g_{7/2} \to 2f_{7/2}(6.2\%)$	$2d_{3/2} \to 3p_{1/2}(1.7\%)$	$2d_{5/2} \to 3p_{3/2}(3.5\%)$
$2d_{3/2} \to 3p_{3/2}(5.5\%)$	$2d_{5/2} \to 3p_{3/2}(1.5\%)$	$1g_{7/2} \to 2f_{5/2}(1.9\%)$
$1g_{7/2} \to 2f_{5/2}(3.7\%)$	$3s_{1/2} \to 3p_{3/2}(1.4\%)$	$1g_{7/2} \to 1h_{9/2}(1.5\%)$
$2d_{5/2} \to 2f_{7/2}(2.0\%)$		
$2d_{3/2} \to 2f_{5/2}(1.6\%)$		

$(\bar{X}^2_{\mu\nu} - \bar{Y}^2_{\mu\nu} = 0.98)$ is $\nu 3p_{3/2} \otimes \nu 2d_{5/2}(\mathcal{E}_\mu = 0.618$ MeV, $\bar{v}^2_\mu = 0.78)$, and at $E = 3.501$ MeV it is $\nu 2d_{5/2} \otimes \nu 2f_{7/2}(\mathcal{E}_\mu = 2.860$ MeV, $\bar{v}^2_\mu = 0.1 \times 10^{-3})$, with $\bar{X}^2_{\mu\nu} - \bar{Y}^2_{\mu\nu} = 0.94$. The proton two-quasiparticle configuration with the largest amplitude has $\bar{X}^2_{\mu\nu} - \bar{Y}^2_{\mu\nu} = (0.2 - 0.3) \times 10^{-2}$.

In Ni, a low-energy peak rises suddenly at ^{80}Ni (Fig. 18). The transition densities to the states in the peak, shown in Fig. 25, are similar to those of the neutron-rich Ca isotopes. The density in ^{98}Ni, at the drip line, is similar though larger, with little collectivity. In Sn there is no sudden increase in the low-energy peak around $N = 82$ (see Fig. 19). Figure 26 shows the transition densities to low-energy states in three isotopes around $N = 82$. Here the proton contributions stretch to larger radii than in Ca or Ni, even though they are dwarfed by the neutron tails there. These states are somewhat more collective than Ni. In ^{132}Sn, for example, the largest squared amplitudes in the two states shown are 0.68 (in the state at 7.224 MeV) and 0.28 (in the state at 8.014 MeV). The other Skyrme interactions give very similar results, both in the IS and IV channels.

The increased collectivity in ^{132}Sn is interesting because other groups have done calculations there [8,21,23,24], particularly in the IV channel. In our calculations the low-lying 1^- IV resonance is not as strong as in the relativistic RPA [8] or QRPA [21]; those models yield 5% of the energy-weighted strength below 10 MeV in ^{132}Sn, whereas we have only about 1%. To see why, we compare in Table II the composition of two of our strong low-energy SkM* states, at 8.0 and 8.6 MeV with 0.8% of the EWSR together, with one of theirs, at 8.6 MeV [8] with 1.4% of the EWSR. The largest two-quasineutron component of our 8.6 MeV state is the same as theirs, and the degree of collectivity in our 8.0 MeV state is comparable to theirs. We suspect that the difference in strength is related to the structure of the single-particle wave functions rather than a collective enhancement. Reference [21] reports that the neutron radius in this nucleus is 0.34 fm larger than the proton radius, whereas we find a difference of only 0.23 fm. The larger neutron skin in the relativistic mean field may be responsible for the stronger IV pygmy resonance.

Near the drip line we find some collectivity in low-lying IV states as well. Table III shows the detailed composition of four strong low-energy states in ^{174}Sn. The strongest is more collective than any states in the 0^+ channels, with no

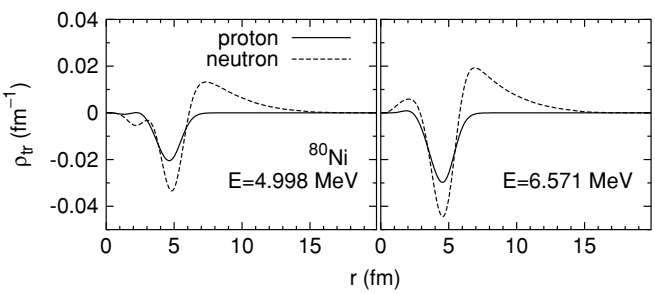

FIG. 25. Transition densities to the excited states in the low-energy peak of the IS 1^- strength function of ^{80}Ni.

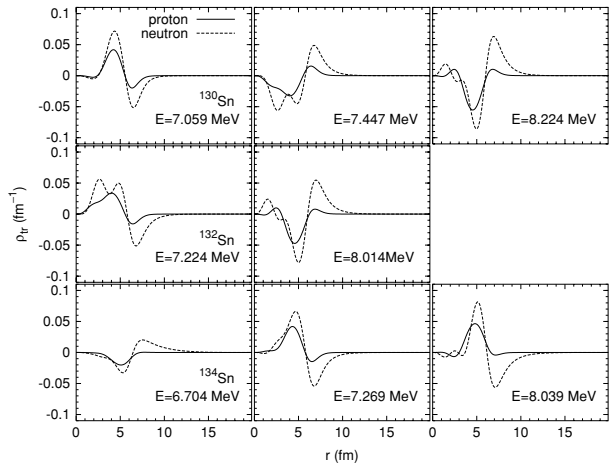

FIG. 26. Transition densities to the excited states in the low-energy peak of the IS 1^- strength function of ^{130}Sn (upper panels), ^{132}Sn (middle panels), and ^{134}Sn (lower panels).

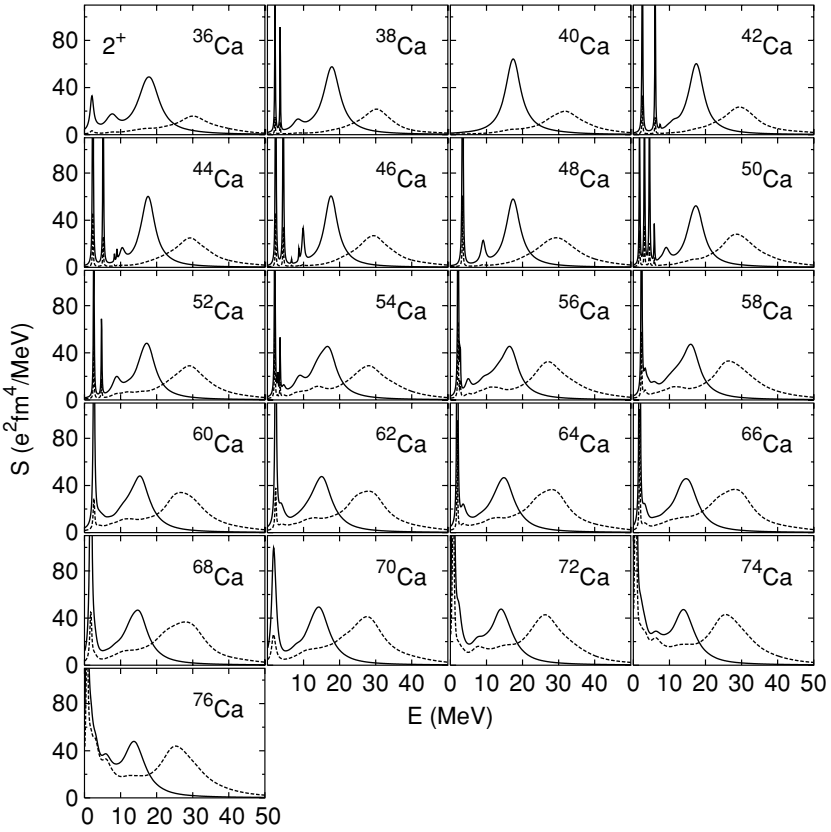

FIG. 27. IS (solid) and IV (dashed) 2^+ strength functions in even Ca isotopes (SkM*).

single component representing more than 50% of the state. The second strongest is essentially a two-quasiparticle state, with the other two states somewhere in the middle. This decomposition and the comparison of the two calculations in ^{132}Sn illustrate perhaps the main point of this article: The extended neutron skin means that there is no clear correlation between strength and collectivity in neutron-rich nuclei.

D. 2^+ channels

1. 2^+ *strength functions*

The strength functions in the 2^+ channels are qualitatively different from those in the lower-multipole channels. In Ca, for example (Fig. 27), all isotopes except $N = 20$ have considerable low-energy strength, in many instances because

TABLE III. Two quasineutron components of strong low-energy IV 1^- excited states in ^{174}Sn. The percentages are the differences between the squared RPA forward amplitudes and backward amplitudes; only those larger than 1% are shown. The first row contains the excitation energy and the second the strength. Components without arrows have predominantly two-particle character; the others are closer to particle-hole excitations.

4.252 MeV $1.64\,e^2$ fm^2	4.799 MeV $0.91\,e^2$ fm^2	5.846 MeV $0.89\,e^2$ fm^2	6.204 MeV $0.76\,e^2$ fm^2
$2f_{5/2} \rightarrow 4d_{3/2}$(46.6%)	$4p_{3/2} \rightarrow 3d_{5/2}$(91.8%)	$3p_{1/2} \rightarrow 5s_{1/2}$(67.0%)	$1h_{9/2} \rightarrow 2g_{7/2}$(44.1%)
$3p_{1/2} \rightarrow 4d_{3/2}$(24.8%)	$4p_{3/2} \rightarrow 4d_{3/2}$(1.9%)	$2g_{7/2} \rightarrow 2f_{5/2}$(24.9%)	$(3f_{7/2})(3d_{5/2})$(38.3%)
$4p_{3/2} \rightarrow 4s_{1/2}$(22.5%)	$(4s_{1/2})(4p_{1/2})$(1.4%)	$1i_{13/2} \rightarrow 1j_{15/2}$(1.1%)	$1i_{13/2} \rightarrow 1j_{15/2}$(4.2%)
$2f_{5/2} \rightarrow 3d_{5/2}$(2.5%)	$2f_{5/2} \rightarrow 4d_{3/2}$(1.1%)		$2g_{9/2} \rightarrow 3f_{7/2}$(3.4%)
			$2f_{7/2} \rightarrow 2g_{9/2}$(1.7%)
			$2f_{5/2} \rightarrow 2g_{7/2}$(1.5%)

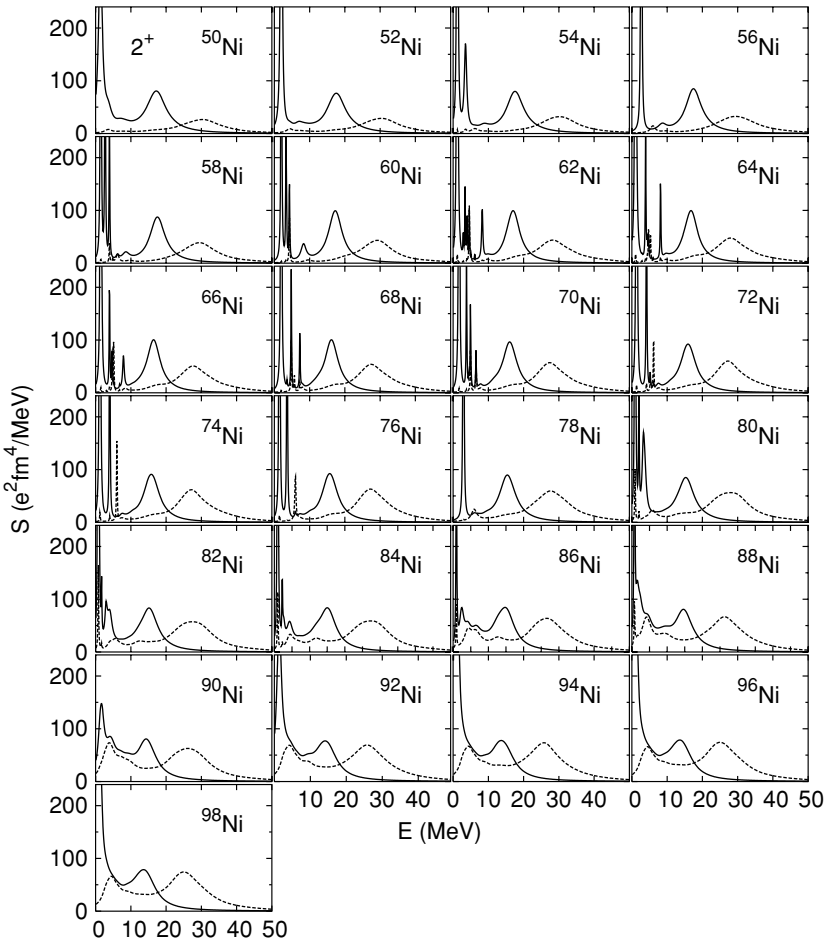

FIG. 28. The same as Fig. 27 but for Ni isotopes.

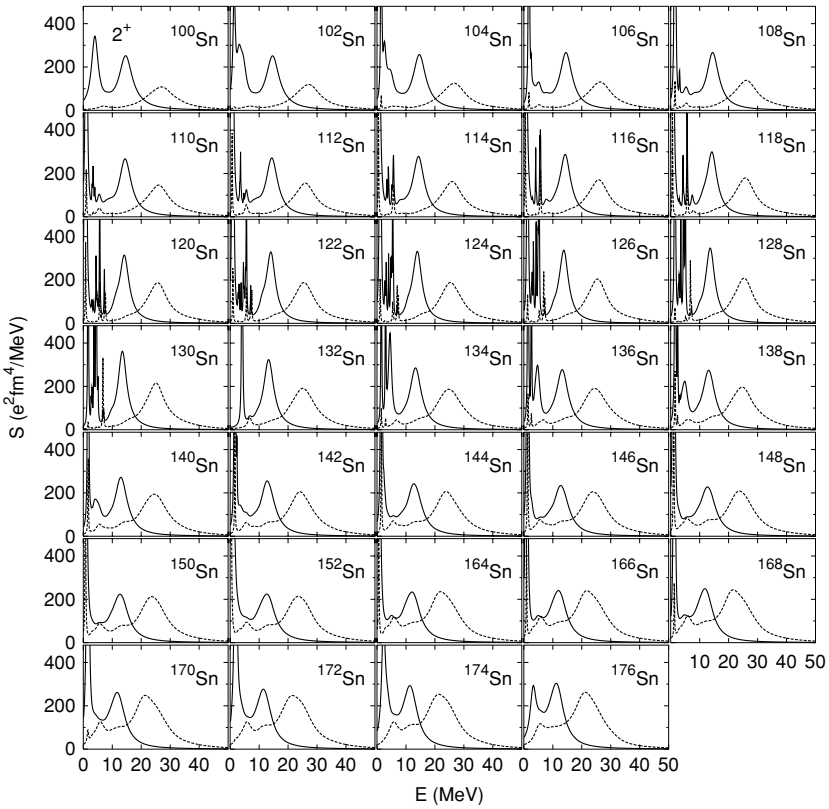

FIG. 29. The same as Fig. 27 but for Sn isotopes.

of sharp quadrupole vibrations.[6] The low-energy strength grows with N, but unlike in the 0^+ channel, both neutrons and protons are involved in the transitions to these states, even near the drip line, because the IS peaks are much larger than the IV peaks, for all Skyrme interactions, in all isotopes except ^{76}Ca. Even there, the IS strength to the low-energy peak with SkM* is 256 e^2 fm^4 and the IV strength only 136 e^2 fm^4.

The 2^+ strength functions in Ni (Fig. 28) are similar, though with two differences: all the isotopes, including those at closed shells, have low-energy peaks, and for $^{90-98}$Ni the IV peak is at a different energy than the IS peak. The lowest-lying peak seems to be nearly pure IS, like the familiar surface-quadrupole vibrations in stable nuclei.

SLy4 puts the drip line at ^{88}Ni, much closer to stability, and in isotopes close to ^{88}Ni it puts the IS and IV peaks at about the same location. In the lighter ($A \geqslant 80$) Ni isotopes, the lowest peak always has a little bit of IV strength mixed with the IS strength, as with SkM*. In ^{80}Ni (SkM*), the IV strength in the peak at 400 keV is 5% of the IS strength.

Things are quite similar in Sn (Fig. 29); for $^{134-170}$Sn the lowest-energy peak has both IS and the IV components but in $^{172-176}$Sn it has no IV component. The other interactions give the same results near the neutron drip line, indicating again that proton excitations are important in these modes everywhere.

The predictions for the IS W_E in Ca (Fig. 30) show that SLy4 evinces slightly more of a closed shell (a small kink in the 10-MeV curve) at $N = 40$ than does SkM*, whereas showing less of a shell effect at $N = 28$ (no small kink in the 20-MeV curve). Similar differences in shell-strength among the Skyrme interactions are apparent in the Ni IS W_E curves (Fig. 31). The IS W_E for Sn (Fig. 32) indicate that SkP has more low-energy strength ($N > 82$) than the other parameter sets.

As was the case in the 0^+ and 1^- channels, the IV W_E are monotonic with N with no obvious kinks but depends slightly on the interaction.

[6]Reference [14] shows no low-energy 2^+ peaks in calculated ^{60}Ca strength functions, probably because pairing is neglected so that nucleus is semimagic.

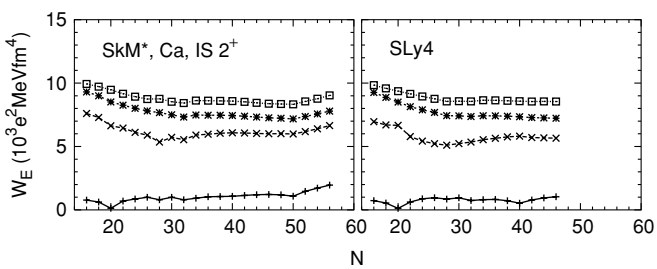

FIG. 30. The same as Fig. 5 but for the 2^+ channel.

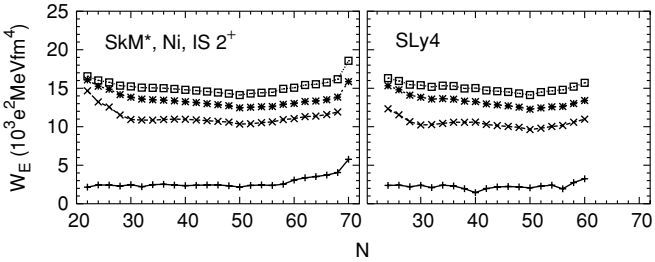

FIG. 31. The same as Fig. 7 but for the 2^+ channel.

2. 2^+ *transition densities*

Figures 27–29 showed that at the neutron drip line the IS and IV strength functions in Ni and Sn have distinct low-energy peaks (though the IS strength is always larger, even at the low energy IV peak), whereas in Ca the peaks coincided. With SkM*, the IS strength of the large low-energy peak at $E = 0.096$ MeV in ^{98}Ni is 92% of the total strength (8.9% of the EWSR) and that of the peak at $E = 0.713$ MeV in ^{176}Sn is 23% of the total strength (2.2% of the EWSR). In Fig. 33 we compare the transition densities of the states in these low-energy peaks with those in ^{76}Ca. As Fig. 27 suggests, though the protons play a role, the neutrons are proportionately more important in Ca and do not seem to correlate with the protons. In ^{98}Ni and ^{176}Sn, by contrast, the neutrons and protons are completely in phase (as they must be if the IV strength is negligible).

The other Skyrme interactions bear out these conclusions, though in the SLy4 calculation of the drip-line Ca isotope the ratio of proton transition density to neutron transition density is larger than that with SkM* (shown in the left panel of Fig. 33). In all nuclei near the neutron drip line, the states in low-energy peaks are mostly above neutron-emission threshold, yet the neutron tails cut off at much smaller radii than do those in the 0^+ and 1^- channels. In addition, the transition densities in those other channels generally have a node at about $r = 5$ fm, whereas the 2^+ transition densities show no such feature.

We put off for just a moment the obvious question of whether these low-lying IS peaks are familiar quadrupole vibrations and turn briefly to the IV channel. Figure 34 shows the transition densities to states in the low-energy IV strength-function peak in ^{176}Sn and ^{98}Ni. The states in ^{176}Sn display remarkably IS character, despite being at the peak of the IV distribution. The fact that the IV distribution peaks there is a little misleading because the IS strength is still considerably larger, even though it is larger still at lower energies. We get some IV strength because the ratio of the transition density of protons to that of neutrons is not exactly equal to Z/N [see Eq. (3)].

Returning to the IS strength, we note, in accord with Fig. 33, that the transitions appear more collective in the Ni and Sn drip-line isotopes than in that of Ca. The component with the largest amplitude ($\bar{X}^2_{\mu\nu} - \bar{Y}^2_{\mu\nu} = 0.81$) in the state at $E = 0.713$ MeV of ^{76}Ca is $\nu 3s_{1/2}(\mathcal{E}_\mu = 0.355$ MeV, $\bar{v}^2_\mu = 0.65) \otimes \nu 2d_{5/2}(\mathcal{E}_\mu = 0.618$ MeV, $\bar{v}^2_\mu = 0.78)$ and that with the second largest ($\bar{X}^2_{\mu\nu} - \bar{Y}^2_{\mu\nu} = 0.16$) is $\{\nu 2d_{5/2}\}^2$. This is still

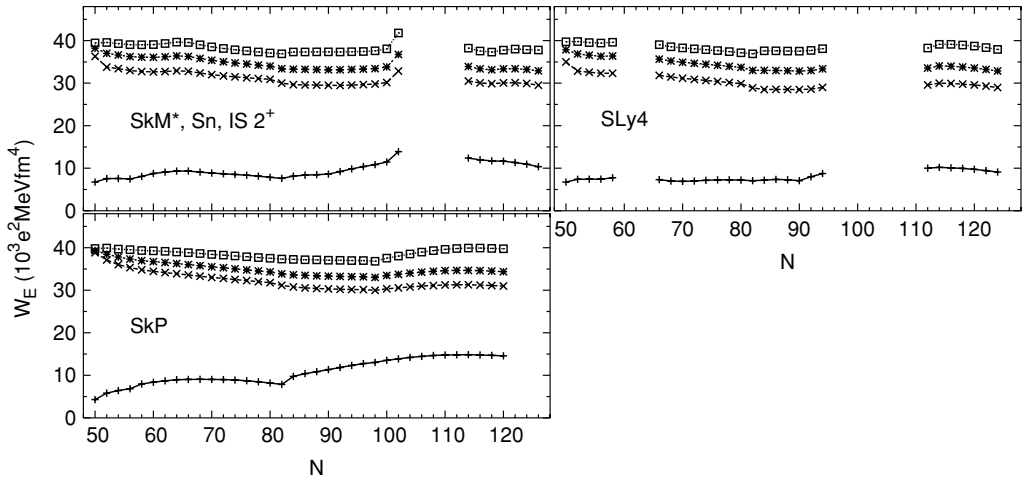

FIG. 32. The same as Fig. 8 but for the 2^+ channel.

a predominantly two-quasiparticle excitation. By contrast, the components of the state at $E = 0.096$ MeV in ^{98}Ni with the largest amplitudes are

$$\{\nu 1h_{11/2}(\mathcal{E}_\mu = 1.415\ \text{MeV}, \bar{v}_\mu^2 = 0.27)\}^2,\ \bar{X}_{\mu\nu}^2 - \bar{Y}_{\mu\nu}^2 = 0.35,$$
$$\{\nu 1g_{7/2}(\mathcal{E}_\mu = 1.350\ \text{MeV}, \bar{v}_\mu^2 = 0.59)\}^2,\ \bar{X}_{\mu\nu}^2 - \bar{Y}_{\mu\nu}^2 = 0.30,$$
$$\pi 2p_{3/2}(\mathcal{E}_\mu = 2.352\ \text{MeV}, \bar{v}_\mu^2 = 0)$$
$$\otimes \pi 1f_{7/2}(\mathcal{E}_\mu = 2.222\ \text{MeV}, \bar{v}_\mu^2 = 1),\ \bar{X}_{\mu\nu}^2 - \bar{Y}_{\mu\nu}^2 = 0.12.$$

Although still not very collective, this state is more so than its counterpart in Ca. (^{98}Ni may be in the spherical-deformed transition region.)

In ^{176}Sn, a state with large IS strength lies at $E = 3.228$ MeV. This state, interestingly, is not the lowest 2^+ excitation. The component of this state with the largest amplitude is (Fig. 33) $\nu 2g_{9/2}(\mathcal{E}_\mu = 1.477\ \text{MeV}, \bar{v}_\mu^2 = 0) \otimes \nu 1i_{13/2}(\mathcal{E}_\mu = 2.475\ \text{MeV}, \bar{v}_\mu^2 = 1.00)$, $(\bar{X}_{\mu\nu}^2 - \bar{Y}_{\mu\nu}^2 = 0.79)$ and that with the next largest is $\pi 2d_{5/2}(\mathcal{E}_\mu = 3.654\ \text{MeV}, \bar{v}_\mu^2 = 0) \otimes \pi 1g_{9/2}(\mathcal{E}_\mu = 2.276\ \text{MeV}, \bar{v}_\mu^2 = 1)$, $(\bar{X}_{\mu\nu}^2 - \bar{Y}_{\mu\nu}^2 = 0.09)$. This excitation is mainly a single neutron particle and neutron hole. Still, the proton contribution is much larger than that in other channels at the neutron drip line. This excited state has 23.7% of the total IS strength and 8.6% of the EWSR. We see both in this channel, once again, that the large transition strength near the neutron drip line does not always indicate the coherent contributions of many two-quasiparticle excitations (i.e., collectivity). Yet the transition densities make these strong low-lying states, particularly in Ni and Sn, look very much like the surface vibrations that characterize nuclei closer to stability.

Normally, the lowest 2^+ states are vibrational. To get a better handle on the degree to which these states can be called vibrations, we show in Fig. 35 the energy, transition probability $B(E2; 0^+ \to 2^+)$, and largest $\bar{X}_{\mu\nu}^2 - \bar{Y}_{\mu\nu}^2$ for neutrons in the lowest-energy 2^+ states of Ca, Ni, and Sn. The Ca panel shows, first, that we do not reproduce experimental data very well except in a few nuclei and, second, that the states are dominated by a single two-quasiparticle excitation for $N \leqslant 34$. For $34 \leqslant N \leqslant 40$ something peculiar happens: when the energy increases, so does the $B(E2; 0^+ \to 2^+)$, and vice versa, with the largest $\bar{X}_{\mu\nu}^2 - \bar{Y}_{\mu\nu}^2$, a measure of collectivity, varying irregularly. In nuclei with collective vibrations transition strength is usually correlated inversely with energy [42,43]; we see the opposite here. Near the neutron drip line of Ni, the classic signs of increasing quadrupole collectivity—decreasing energy, rising $B(E2; 0^+ \to 2^+)$, and decreasing maximum $\bar{X}_{\mu\nu}^2 - \bar{Y}_{\mu\nu}^2$—are all present. The Sn isotopes look much more familiar, exhibiting the usual trends, except at the magic numbers. And the states close to

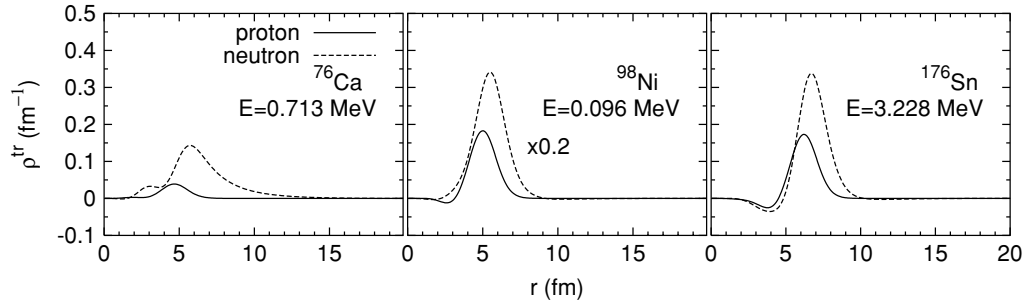

FIG. 33. Transition densities to the excited states in the low-energy peak of the IS 2^+ strength functions in the neutron-drip-line nuclei (with SkM*) ^{76}Ca, ^{98}Ni, and ^{176}Sn. Both proton and neutron curves are reduced by a factor of 5 in ^{98}Ni to fit on the figure.

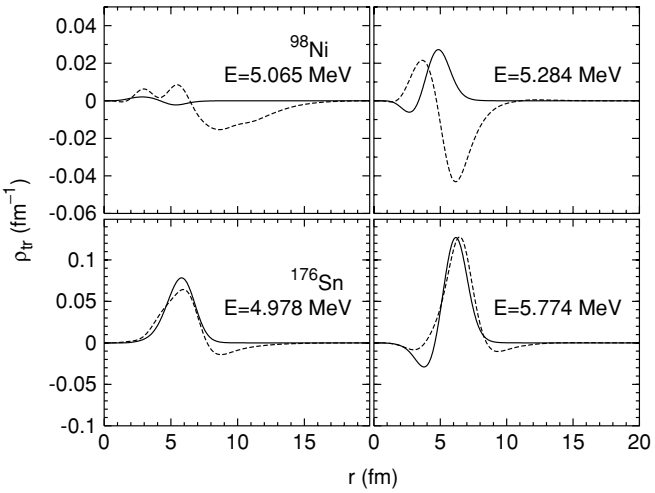

FIG. 34. Transition densities to the excited states in the low-energy peak of the IV 2^+ strength functions (SkM*) in ^{98}Ni (upper panels) and ^{176}Sn (lower panels).

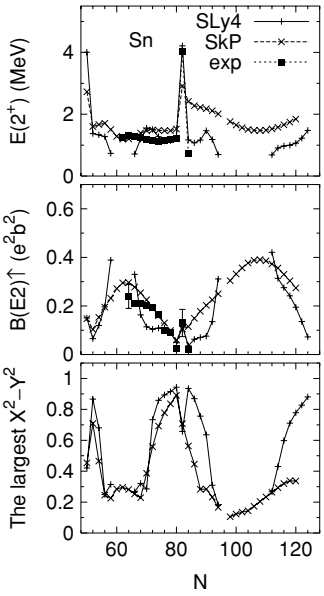

FIG. 36. The same as Fig. 35 but for Sn only, SLy4 and SkP.

the drip line with $96 < N < 124$ are as classically collective as (or more so than) those in more stable isotopes with $56 < N < 68$.

Finally we show the interaction dependence of the collectivity measures for the lowest 2^+ states in Sn (the easiest chain to understand) in Fig. 36. In the midshell region, the energies are low, the $B(E2; 0^+ \rightarrow 2^+)$'s are high, and the largest amplitudes low, as expected from systematics in stable nuclei in regions of large dynamical deformation. The values of these quantities depend significantly on the interaction, however. Ca and Ni show similar behavior but with more irregularities.

IV. CONCLUSION

The feature that leaps out of our calculations is the enhancement of low-energy strength as the neutron drip line is approached. It is present in all multipoles (and is most pronounced in the IS 1^- channel, where the transition operator contains a factor r^3), with all Skyrme interactions, and in every isotopic chain, beginning just after a closed neutron shell. Interestingly, the recent measurement of an IV 1^- strength function at GSI shows a low-energy peak before a closed shell in ^{130}Sn. This may be due to correlations not included in the QRPA.

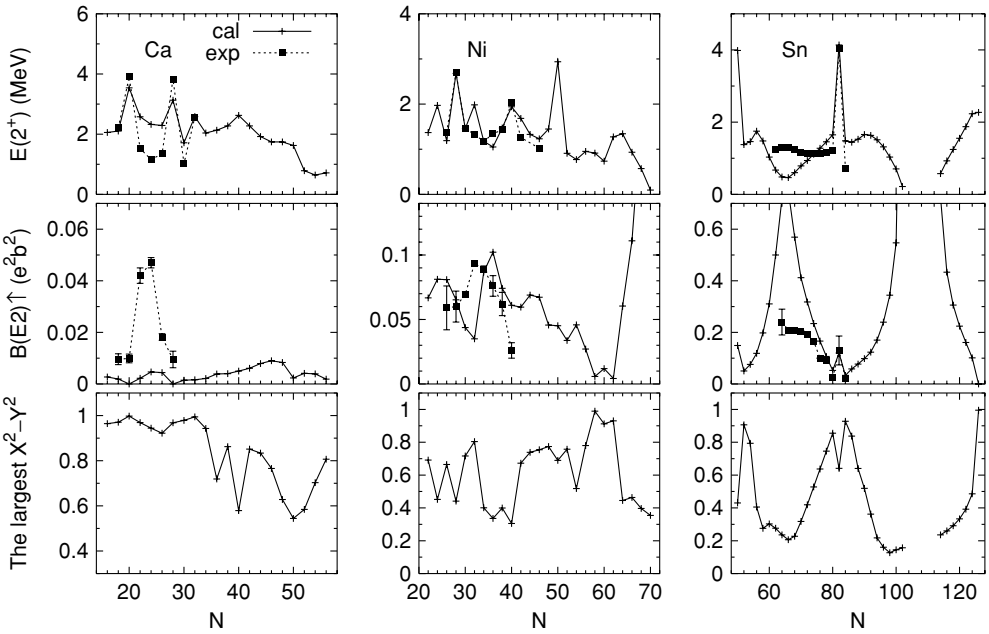

FIG. 35. N dependence of the energy (upper), $B(E2; 0^+ \rightarrow 2^+)$ (middle), and largest $\bar{X}^2_{\mu\nu} - \bar{Y}^2_{\mu\nu}$ (lower) of the lowest 2^+ states in Ca, Ni, and Sn, with SkM*. Experimental data are also shown where available [43].

Remarkably, it is hard to tell by looking at strength distributions and transition densities how collective the low-lying states are. By analyzing our wave functions, we determined that in the 0^+ channel, the predicted low-energy peaks are nearly always created essentially entirely by a single two-quasineutron configuration. In retrospect, this is not surprising given the relatively low number of two-quasineutron states with $J = 0$, and indeed, in the other channels the peaks turn out to be more collective. The 1^- peaks show some neutron collectivity, particularly in Sn, and protons contribute significantly to the transition densities, despite the lack of any individual two-quasiproton configurations with sizable amplitude. In both the 0^+ and 1^- channels the transition densities peak around the rms radius and extend well outside it, allowing individual two-quasineutron configurations to carry large strength.

The transition densities to 2^+ states are different; they have no real nodes and a proton component that is of the same order as the neutron component. The strong low-energy states near the neutron-drip line have transition densities that resemble those of surface vibrations and often are quite collective. But in Ca they are less so, and the usual systematics of vibrations is not universal; in isotopes with $N = 34$–40 energies and $E2$ strengths are correlated in the wrong way. The relationship among collectivity, strength, and transition density is complicated in neutron-rich nuclei.

Some of the most significant differences in the predictions of the three Skyrme interactions we used are in static properties: the locations of the neutron drip line and quadrupole-deformed regions. But some dynamical properties also depend significantly on the interaction, most notably (and easiest to measure) the energies of and transition strengths to the lowest 2^+ states near regions of deformation and the total energy-weighted IV strength.

This article, in a way, is a catalog of predicted dynamic properties of nuclei near the drip line. For the most part we have not offered simple explanations for the anomalies that appear. That, we hope, will be the subject of a future article.

ACKNOWLEDGMENTS

This work was supported in part by the U.S. Department of Energy under grant DE-FG02-97ER41019. We used computers belonging to the National Center for Computational Sciences at Oak Ridge National Laboratory and Information Technology Services at University of North Carolina at Chapel Hill. Parts of this research were done when one of us (J.T.) was at the University of North Carolina at Chapel Hill and at RIKEN.

APPENDIX: TRANSITION DENSITY

The transition density is defined by

$$\rho^q_{\rm tr}(\boldsymbol{r};k) = \langle k| \sum_{i=1}^{N\,{\rm or}\,Z} \delta(\boldsymbol{r}-\boldsymbol{r}_i)|0\rangle, \tag{A1}$$

where $|0\rangle$ and $|k\rangle$ denote the ground and excited states of the system, and $\boldsymbol{r}_i$ in the right-hand side is an operator acting on the nucleon i. The transition density is evaluated in the QRPA (we omit q) as

$$\begin{aligned}\rho_{\rm tr}(\boldsymbol{r};k) = \sum_{K<K'} \big\{ & X^{k*}_{KK'}[\psi^\dagger_{K'}(\boldsymbol{r})\psi_{\bar K}(\boldsymbol{r})u_{K'}v_K \\ & - \psi^\dagger_K(\boldsymbol{r})\psi_{\bar K'}(\boldsymbol{r})u_K v_{K'}] \\ & - Y^{k*}_{KK'}[\psi^\dagger_{\bar K'}(\boldsymbol{r})\psi_K(\boldsymbol{r})v_{K'}u_K - \psi^\dagger_{\bar K}\psi_{K'}(\boldsymbol{r})v_K u_{K'}]\big\},\end{aligned} \tag{A2}$$

where $X^k_{KK'}$ and $Y^k_{KK'}$ are the forward and backward amplitudes of the QRPA solution k (see Appendix A of Ref. [30]), and $\psi_K(\boldsymbol{r})$ stands for a single-particle canonical-basis wave function. The uv factors associated with the basis are represented by u_K and v_K. Assuming spherical symmetry for the system and using

$$\psi_K(\boldsymbol{r}) = \sum_{m\sigma} R_\mu(r) Y_{ll_z}(\Omega)\big\langle ll_z \tfrac{1}{2}\sigma\,|\,jm\big\rangle\big|\sigma\big\rangle, \tag{A3}$$

with $K = (\mu m) = (nljm)$ a set of quantum numbers, $R_\mu(r)$ a radial wave function, and $|\sigma\rangle$ a spin wave function, one can derive

$$\begin{aligned}\rho_{\rm tr}(\boldsymbol{r};k) = & \sum_{\mu\leqslant\mu'} \frac{1}{\sqrt{1+\delta_{\mu\mu'}}}\sqrt{(2j+1)(2j'+1)}R_{\mu'}(r)R_\mu(r) \\ & \times (-)^{j+\frac{1}{2}}\frac{1}{\sqrt{4\pi}}\begin{pmatrix} j' & j & J_k \\ -1/2 & 1/2 & 0\end{pmatrix} \\ & \times \frac{1}{2}[1+(-)^{l'+l+J_k}]Y^*_{J_kM_k}(\Omega)[(-)^{J_k}v_{\mu'}u_\mu \\ & + v_\mu u_{\mu'}]\big[\bar Y^k_{\mu\mu'} + (-)^{J_k}\bar X^k_{\mu\mu'}\big],\end{aligned} \tag{A4}$$

where $\mu' = (n'j'l')$, and J_k denotes the angular momentum of the state k. $\bar X^k_{\mu\mu'}$ and $\bar Y^k_{\mu\mu'}$ are the forward and backward amplitudes in the spherical representation.

[1] A. C. Hayes and D. Strottman, Phys. Rev. C **42**, 2248 (1990).
[2] J. S. Al-Khalili and J. A. Tostevin, Phys. Rev. Lett. **76**, 3903 (1996).
[3] M. Tohyama, Phys. Lett. **B323**, 257 (1994).
[4] M. Yokoyama, T. Otsuka, and N. Fukunishi, Phys. Rev. C **52**, 1122 (1995).
[5] F. Catara, E. G. Lanza, M. A. Nagarajan *et al.*, Nucl. Phys. **A624**, 449 (1990).
[6] I. Hamamoto, H. Sagawa, and X. Z. Zhang, Phys. Rev. C **57**, R1064 (1998).
[7] I. Hamamoto, H. Sagawa, and X. Z. Zhang, Nucl. Phys. **A648**, 203 (1999).
[8] D. Vretenar, N. Paar, P. Ring *et al.*, Nucl. Phys. **A692**, 496 (2001).
[9] G. Colò and P. F. Bortignon, Nucl. Phys. **A696**, 427 (2001).
[10] M. Matsuo, K. Mizuyama, and Y. Serizawa, Phys. Rev. C **71**, 064326 (2005).

[11] H. Sagawa and T. Suzuki, Phys. Rev. C **59**, 3116 (1999).
[12] Y. Suzuki, K. Ikeda, and H. Sato, Prog. Theor. Phys. **83**, 180 (1990).
[13] J. Chambers, E. Zaremba, J. P. Adams, and B. Castel, Phys. Rev. C **50**, R2671 (1994).
[14] H. Sagawa and H. Esbensen, Nucl. Phys. **A693**, 448 (2001).
[15] G. Tertychny, V. Tselyaev, S. Kamerdzhiev *et al*., nucl-th/0603051.
[16] T. Hartmann, M. Babilon, S. Kamerdzhiev, E. Litvinova, D. Savran, S. Volz, and A. Zilges, Phys. Rev. Lett. **93**, 192501 (2004).
[17] S. Goriely and E. Khan, Nucl. Phys. **A706**, 217 (2003).
[18] S. Goriely, E. Khan, and M. Samyn, Nucl. Phys. **A739**, 331 (2004).
[19] N. Paar, P. Ring, T. Niksić, and D. Vretenar, Phys. Rev. C **67**, 034312 (2003).
[20] D. Vretenar, T. Niksić, N. Paar *et al*., Nucl. Phys. **A731**, 281 (2004).
[21] N. Paar, T. Niksić, D. Vretenar *et al*., Phys. Lett. **B606**, 288 (2005).
[22] D. Vretenar, A. V. Afanasjev, G. Lalazissis *et al*., Phys. Rep. **409**, 101 (2005).
[23] D. Sarchi, P. F. Bortignon, and G. Colò, Phys. Lett. **B601**, 27 (2004).
[24] N. Tsoneva, H. Lenske, and C. Stoyanov, Phys. Lett. **B586**, 213 (2004).
[25] I. Hamamoto, H. Sagawa, and X. Z. Zhang, Phys. Rev. C **56**, 3121 (1997).
[26] I. Hamamoto, H. Sagawa, and X. Z. Zhang, Phys. Rev. C **53**, 765 (1996).
[27] G. Colò, P. F. Bortignon, D. Sarchi *et al*., Nucl. Phys. **A722**, 111c (2003).
[28] J. Piekarewicz, Phys. Rev. C **73**, 044325 (2006).
[29] P. Adrich, A. Klimkiewicz, M. Fallot *et al*., Phys. Rev. Lett. **95**, 132501 (2005).
[30] J. Terasaki, J. Engel, M. Bender, J. Dobaczewski, W. Nazarewicz, and M. Stoitsov, Phys. Rev. C **71**, 034310 (2005).
[31] J. Dobaczewski, H. Flocard, and J. Treiner, Nucl. Phys. **A422**, 103 (1984).
[32] J. Dobaczewski, W. Nazarewicz, T. R. Werner, J. F. Berger, C. R. Chinn, and J. Decharge, Phys. Rev. C **53**, 2809 (1996).
[33] P. Ring and P. Schuck, *The Nuclear Many-Body Problem* (Springer-Verlag, Berlin, 1980).
[34] T. Lesinski, K. Bennaceur, T. Duguet, and J. Meyer, nucl-th/0607065.
[35] J. Terasaki and J. Engel, nucl-th/0603062.
[36] J. Bartel, P. Quentin, M. Brack *et al*., Nucl. Phys. **A386**, 79 (1982).
[37] E. Chabanat, P. Bonche, P. Haensel *et al*., Nucl. Phys. **A635**, 231 (1998).
[38] P. F. Bortignon, A. Bracco, and R. A. Broglia, *Giant Resonances, Nuclear Structure at Finite Temperature* (Harwood, Amsterdam, 1998).
[39] G. Colò, N. V. Giai, J. Meyer, K. Bennaceur, and P. Bonche, Phys. Rev. C **70**, 024307 (2004).
[40] J. Terasaki, J. Engel, W. Nazarewicz, and M. Stoitsov, Phys. Rev. C **66**, 054313 (2002).
[41] G. Audi and A. H. Wapstra, Nucl. Phys. **A595**, 409 (1995).
[42] L. Grodzins, Phys. Lett. **2**, 88 (1962).
[43] S. Raman, C. W. Nestor Jr., and P. Tikkanen, At. Data Nucl. Data Tables **78**, 1 (2001).